ELSEVIER

Contents lists available at ScienceDirect

### Journal of the European Ceramic Society

journal homepage: www.elsevier.com/locate/jeurceramsoc



# Quantifying the efficiency of reactions between silicate melts and rare earth aluminate-zirconate T/EBC materials



Eeshani P. Godbole a, Nethmi Hewage a, Anette von der Handt b, David L. Poerschke a,\*

- a Department of Chemical Engineering and Materials Science, University of Minnesota, Minneapolis, MN, USA
- b Department of Earth Sciences, University of Minnesota, Minneapolis, MN 55455, USA

#### ARTICLE INFO

Keywords: T/EBCs CMAS Apatite

Fluorite

#### ABSTRACT

The durability of thermal and environmental barrier coatings (T/EBCs) exposed to molten calcium magnesium aluminosilicate (CMAS) deposits depends on the nature of reactions between the coatings and deposits. These reactions consume the melt, and the crystallization products can block porosity that otherwise facilitates melt infiltration. The ideal reactions rapidly crystallize the melt with a small amount of dissolved T/EBC. This work compares the relative efficiency of reaction products reported in the literature to those formed on four prospective T/EBC materials based on multi-phase combinations of Gd- or Y-zirconates with GdAlO $_3$ , YAlO $_3$ , Gd $_4$ Al $_2$ O $_9$ , or Y $_4$ Al $_2$ O $_9$ . The results show that adding the aluminates to the zirconate materials promotes Gd- or Y-based aluminosilicates garnet and cuspidine crystallization, in addition to apatite. These phases effectively crystallize the melt, but the reaction efficiency is reduced compared to reactions with single phase zirconates. The implications for integration of these multiphase materials into T/EBC architectures are discussed.

#### 1. Introduction

Interactions between ceramic thermal and environmental barrier coatings (TBCs, EBCs), which protect hot-section components in turbine engines, and molten calcium magnesium iron aluminosilicate (CMFAS) deposits shorten coating lifetimes. These deposits form when aerosols ingested into the engines adhere to hot surfaces. At high service temperatures the melts react with the coatings and infiltrate porosity causing thermo-mechanical damage during thermal cycling [1–6]. Increasing coating operating temperatures to improve engine performance and efficiency will require new coating materials to withstand CMFAS attack by variable deposit compositions over a wide temperature range [7,8].

Mitigation strategies often focus on controlling the reactions between the deposit and the coating materials. For porous TBCs, the approach seeks to maximize crystallization to block melt infiltration into the strain-tolerant architectures [3,9,10]. For EBCs, approaches aim to either efficiently convert the melt into a small volume of reaction products with minimal CTE mismatch, or to avoid reactions entirely. Other approaches use sacrificial coating layers that form thin, uniform CMFAS reaction layers that exfoliate while leaving the majority of the coating intact [1,11–14].

The products of the coating-deposit reactions can be divided into three categories: intrinsic crystallization products incorporate ions primarily from just the siliceous deposit, reprecipitation products are formed primarily from ions originating in the coating, and reactive crystallization products incorporate ions from both deposit and coating. Intrinsic and reactive crystallization products are preferred to efficiently consume the melt with minimal coating dissolution. The most-reported reactive crystallization product is a Ca-containing rare earth (RE) silicate with the apatite structure. It forms readily with larger RE cations and Ca-rich deposits, but its less-reliable formation for Ca-lean deposits leads to variable coating performance depending on the CMFAS composition. Research has also identified an aluminosilicate garnet reaction product that is more likely to form upon reaction with coating materials based on smaller RE cations, aluminates or with deposits containing higher concentrations of Mg, Ca, Al, and other oxides [15-24]. The ability of the garnet structure to accommodate a wide range of cations gives it potential for efficient melt consumption, and more consistent reaction response to variable deposit chemistry.

The efficiency of a particular crystallization product in consuming the melt  $(\eta, \text{Eq. 1})$  can be quantified in terms of the sum molar fraction (x) of the cations (i) in the product that are also present in the coating material.

E-mail address: dpoersch@umn.edu (D.L. Poerschke).

 $<sup>^{\</sup>ast}$  Corresponding author.

$$\eta = 1 - \sum_{i} x_i \tag{1}$$

The reprecipitation and intrinsic crystallization efficiency are zero and one, respectively, since all the cations come in from the deposit or the coating. Reactive crystallization falls in between, and those reactions with higher values are more efficient at consuming the melt for a minimum amount of coating dissolution. Although reactive crystallization consumes the melt less efficiently than intrinsic crystallization, the ability of the coating-deposit reactions to raise the liquidus temperature provides benefit.

Fig. 1 compares the reaction efficiency for various reaction products reported in the literature. The garnet crystallization efficiency (Fig. 1(a)) varies considerably depending on the coating material and deposit composition. The crystallization of an Al-rich garnet via reactions with yttrium aluminate perovskite (YAP) is not efficient ( $\eta < 0.25$ ) while other studies showed that reactions with the equivalent Gd-based phase (GAP) have  $\eta \sim$  0.6. Garnet crystallization from RE zirconate and hafnate coating materials is quite efficient, requiring only a small fraction of RE cations from the coating material. In comparison, the formation of ZrO<sub>2</sub>- or HfO<sub>2</sub>-rich fluorite from those materials (Fig. 1(b)) is uniformly inefficient except in rare occasions when CaO incorporation increases  $\eta$ . Likewise, the modest CaO incorporation for apatite crystallization from RE silicate EBC materials such as Y mono- and disilicate (YMS, YDS) results in relatively low efficiency compared to apatite formed via reactions with RE-zirconate, -hafnate, and -oxide coating materials, with  $\boldsymbol{\eta}$ ~ 0.5.

This literature analysis suggests that coating materials designed to promote RE aluminosilicate garnet crystallization could increase the reactive crystallization efficiency. Recent work showed that the addition of alumina (in the form of RE aluminates) to RE zirconate coating materials can shift the reaction equilibria into fields producing significant fractions of garnet [33]. However, questions remain about (i) to what degree the reaction efficiency is reduced by including an additional garnet-stabilizing cation in the coating material and (ii) how the reaction efficiency changes with variations with CMFAS composition. This article addresses these questions based on changes in the reaction sequence and reaction product composition as a function of the RE identity, alumina content in the coating material, and CMFAS composition.

#### 2. Experimental methods

#### 2.1. Materials selection, preparation, and testing

Details of the material selection, preparation, and testing are provided elsewhere [33]. In brief, four compositions in the rare earth oxide rich corner of the REO<sub>1.5</sub>-AlO<sub>1.5</sub>-ZrO<sub>2</sub> systems (Fig. 2) were studied. Each has an 85:15 RE:Zr molar ratio and contains either 10 mol% or 30 mol% AlO<sub>1.5</sub> and either Y or Gd as the RE cation. The  $A_{10}G_{76}Z_{14}^{-1}$  and  $A_{10}Y_{76}Z_{14}$  compositions fall in the phase field containing the ZrO<sub>2</sub>-saturated REO<sub>1.5</sub>, fluorite, and the rare earth aluminum monoclinic (RE<sub>4</sub>Al<sub>2</sub>O<sub>9</sub>).  $A_{30}G_{60}Z_{10}$  and  $A_{30}Y_{60}Z_{10}$  fall in the field containing fluorite and the monoclinic and perovskite aluminates. The model CMFAS compositions were chosen to evaluate the effect of the Ca:Si ratio and the total  $Mg^{2+}$ ,  $Fe^{2+/3+}$  and  $Al^{3+}$  ( $\Sigma$ (MFA)) content on the reactions, and included  $C_{10}M_5F_5A_{10}S_{70}$  (Ca:Si = 0.14,  $\Sigma$ (MFA) = 20 mol%)  $C_{15}M_{12}F_{12}A_{16}S_{45}$  (Ca:Si = 0.33,  $\Sigma$ (MFA) = 40 mol%) and  $C_{31}M_9F_5A_{12}S_{43}$  (Ca:Si = 0.72,  $\Sigma$ (MFA) = 26 mol%). These also span most of the range of reported engine deposit compositions [34]. The

coating materials were synthesized by co-precipitation from mixed metal nitrates, calcined at 1000 °C, ball milled, cold pressed to 13 mm diameter pellets, sintered at 1500 °C for 50 h, and polished to a 1  $\mu m$  finish with SiC papers and then diamond lapping films. The sintered pellets were typically >95% dense without interconnected porosity. The pre-reacted crystalline CMFAS powders were applied to a 4 mm diameter region with a 15 mg/cm² areal loading, and then reacted for 1 h at 1400 °C.

#### 2.2. Characterization

Mounted cross sections of the samples were polished to a 1 µm finish using SiC papers and diamond suspensions. The samples were coated with Pt for high resolution imaging via backscattered scanning electron microscopy (BS SEM, Hitachi SU8230), repolished, and then coated with carbon for quantitative chemical analyses by electron probe microanalysis with wavelength dispersive spectroscopy (EPMA-WDS, JEOL JXA-8530FPlus). Point scans were acquired with a focused beam at 15 kV accelerating voltage and 30 nA beam current. Quantitative X-ray maps were acquired at 150 nA with a map pixel size of 0.25 µm and a dwell time of 150 ms per pixel. This map pixel size provided at least 4 pixels per grain to ensure statistical confidence in the composition of each grain. The uncertainty in measurement from the quantitative EPMA maps is  $\pm$  5 wt% and from the point scans is  $\pm$  1–2 wt%. The background intensity correction was performed using the mean atomic number (MAN) calibration curves [36–38]. Details regarding the EPMA detector set up and standards is given in the Supplementary Information. Data from point analyses was acquired and analyzed using Probe for EPMA software (Probe Software Inc.) [39]. Quantitative X-ray maps were acquired using Probe Image software, pre-processed using Calc-Image (Probe Software Inc.) and analyzed using Surfer (Golden Software). Chemical compositions for individual grains were obtained from the maps by averaging data for each pixel contained entirely within each

#### 3. Results and discussion

#### 3.1. Overview of reaction products

A variety of crystalline reaction products formed (Table 1). Apatite, garnet, and fluorite were the most prevalent crystalline reaction products. Key observations about those phases, which are supported by evidence provided in the following sections, include:

- 1. Apatite often appears near the top of the reaction layer, suggesting that it precipitates from the melt early in the reactions. Most apatite compositions fall near the defect-free stoichiometry  $\text{Ca}_2\text{RE}_8(-\text{SiO}_4)_6\text{O}_2$ , except when small amount of MgO substitutes for CaO in apatite formed with the Ca-lean  $\text{C}_{10}\text{M}_5\text{F}_5\text{A}_{10}\text{S}_{70}$  deposit.
- 2. The garnet compositions vary more between samples. Garnets formed in the Y-based systems incorporate enough Si to replace up to half of the Al in the tetrahedral sites, with coupled Ca, Mg, and Fe substitutions providing charge compensation. The garnets formed in the Gd systems are Al and Zr rich with lower Si solubility than the Y-containing garnets.
- 3. Fluorite was observed as a reaction product in all Y-containing tests but only in four tests with Gd-containing materials. In each case, the fluorite reaction product contained less RE than the fluorite in the coating material, and exhibited limited Ca solubility.
- 4. Cuspidine, a solid solution based on RE<sub>4</sub>Al<sub>2</sub>O<sub>9</sub> with charge-compensating coupled substitution of Ca for RE and Si for Al, was observed in the reaction layers for the  $A_{30}Y_{60}Z_{10}$ ,  $A_{10}Y_{76}Z_{14}$ , and  $A_{10}G_{76}Z_{14}$  samples exposed to  $C_{31}M_9F_5A_{12}S_{43}$ .
- 5. YDS formed when the Y-based materials were exposed to  $C_{10}M_5F_5A_{10}S_{70}.$  The measurements were near the nominal  $Y_2Si_2O_7$

 $<sup>^1</sup>$  Compositions are abbreviated using the first letter of the cation symbol with the mol% of the oxide as a subscript, e.g.,  $A_{10}G_{76}Z_{14}$  is 10 mol%  $AlO_{1.5},\,76$  mol%  $GdO_{1.5}$  and 14 mol%  $ZrO_2$ . The actual compositions  $(A_{10}RE_{76.5}Z_{13.5}$  and  $A_{30}RE_{59.5}Z_{10.5}$  are rounded to the nearest integer mol%.

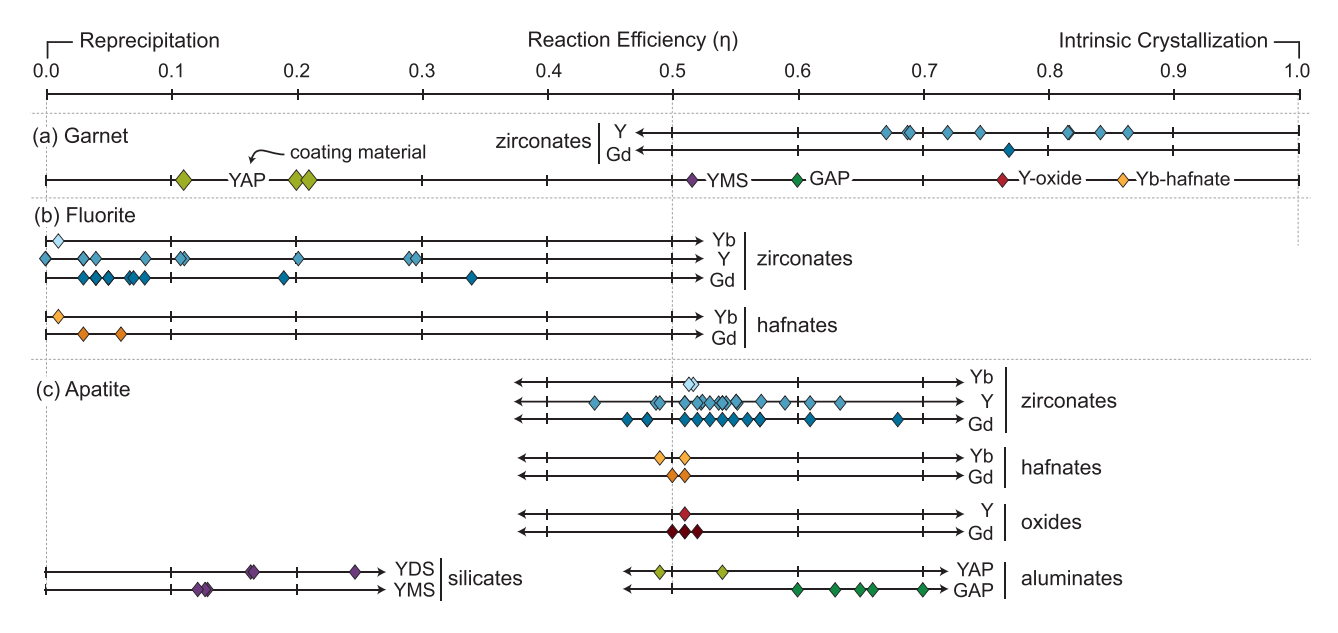


Fig. 1. CMFAS melt consumption reaction efficiency of (a) garnet, (b) fluorite, and (c) apatite reaction products formed upon interaction with a variety of aluminate, silicate, zirconate, and hafnate coating materials.

Values based on compositions reported in Ref. [20-22,25-32].

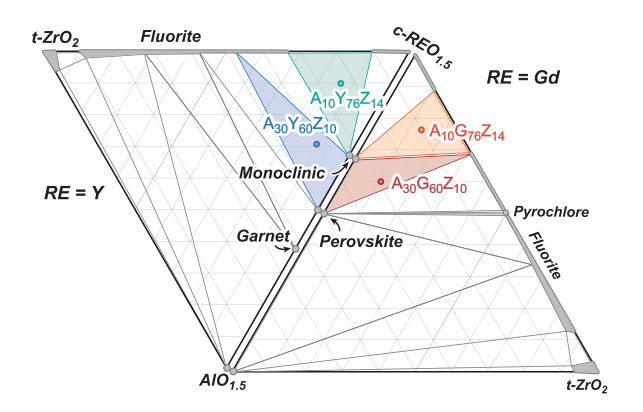


Fig. 2. Calculated 1500 °C isothermal sections for the (Gd/Y)O $_{1.5}$ -AlO $_{1.5}$ -ZrO $_{2}$  systems illustrating the coating material compositions studied. Adapted from Ref. [35].

**Table 1**Summary of the observed reaction products.

•	1		
Phase name	Abbreviation	Prototypical Formula	Type
Apatite	Ap	(Ca,RE,Mg) <sub>4</sub> (RE, Zr) <sub>6</sub> (SiO <sub>4</sub> ) <sub>6</sub> O <sub>2</sub>	Reactive
Garnet	G	(Ca,RE,Zr,Fe) <sub>3</sub> (Mg, Al,Fe) <sub>2</sub> (Si,Fe,Al) <sub>3</sub> O <sub>12</sub>	Reactive
Fluorite	F	(Zr,RE,Ca)O <sub>1,x</sub>	Reprecipitation
Yttrium disilicate	YDS	$Y_2Si_2O_7$	Reactive
Cuspidine	Cus.	(Ca,RE) <sub>4</sub> (Al,Si) <sub>2</sub> O <sub>9.x</sub>	Reactive
Periclase	Peri	MgO	Intrinsic
Glass (Liquid)	L	_	_
Spinel	Sp.	MgAl <sub>2</sub> O <sub>4</sub>	Intrinsic
Cristobalite	Cr	$SiO_2$	Intrinsic
Magnetoplumbite	MP	$GdMgAl_{11}O_{19}$	Reactive
Gadolinium aluminate	GAP	$GdAlO_3$	Reprecipitation

- with modest ( $\sim$ 2 mol%) ZrO<sub>2</sub> solubility. Gadolinium disilicate (GDS) was not observed.
- 6. Reactions with the Gd-containing materials formed spinel (nominally  $(Mg,Fe)(Fe,Al)_2O_4)$  in three samples, magnetoplumbite (nominally  $GdMgAl_{11}O_{19}$ ) in two samples, and periclase (MgO) in one.
- 7. Except for the  $A_{10}Y_{76}Z_{14}$ - $C_{10}M_5F_5A_{10}S_{70}$  test, the residual melt (glass) is limited to small volume fractions between the crystalline grains.

#### 3.2. Reaction Sequences

Upon heating, the deposit melts, the coating material dissolves, and reaction products precipitate. This sequence continues as the reactions progressively consume the coating material until either the melt is exhausted, or equilibrium is established between the residual melt and the coating material. Although 1 h at 1400 °C was sufficient to consume the melt in most cases, the tests are also short enough to limit diffusion and solid-state reactions within the reaction layer. Thus, changes in the prevalence of each reaction product from the outer surface of the reaction layer toward the unreacted material can be used to infer the approximate reaction sequence.

Fig. 3 summarizes the prevalence of each major reaction product through the thickness of a representative region near the center of the reaction layer, as identified based on a combination of BSE contrast, morphology, and EPMA composition maps. The results show that apatite is present throughout the reaction layers, except in the inner portion of the reaction layers formed with the  $C_{31}M_9F_5A_{12}S_{43}$  deposit. This result is counter to the conventional wisdom that Ca-rich deposits are most effective in crystallization of apatite, and is due to a transition toward cuspidine precipitation in those samples. Garnet also forms in every sample, but it tends to appear later in the reaction sequence as  $SiO_2$  is consumed via apatite formation. Fluorite appears through much of the reaction layer except for the Gd-based samples exposed to  $C_{31}M_9F_5A_{12}S_{43}$ , where the  $ZrO_2$  is incorporated into the garnet. Spinel appears in the reaction layer for half of the Gd-containing samples.

Additional details, including discussion of cases where there were notable differences in reaction behavior between the center and the periphery of the reaction zone are provided in the sections that follow. The results are organized separately for the Y- and Gd-containing

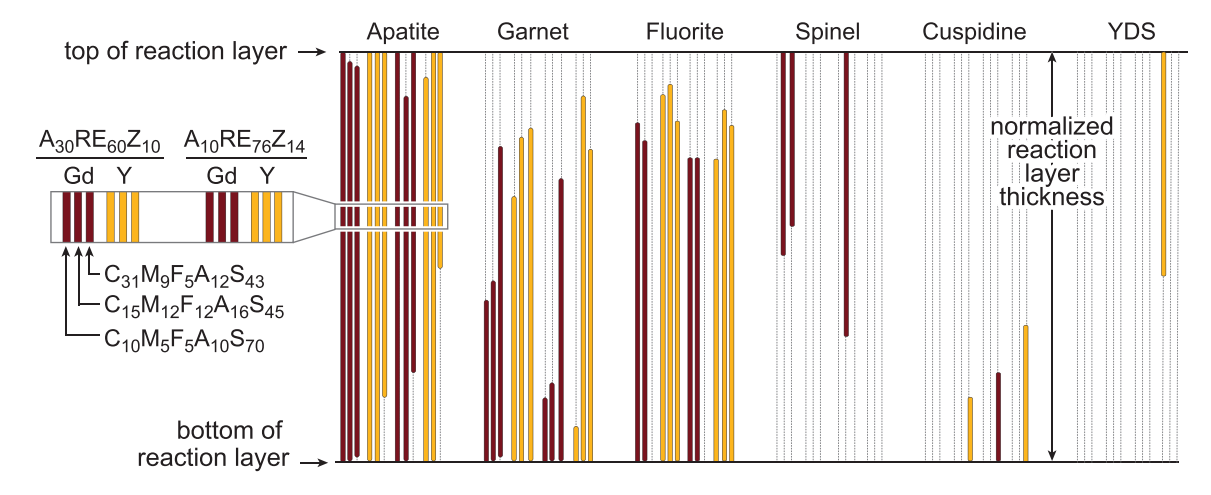


Fig. 3. Distribution of major reaction products through the reaction layer in the center of each sample.

materials and are grouped based on the predominant reaction products. In this presentation, representative BSE micrographs are false colored based on BSE contrast to highlight the different phases. EPMA maps for Zr, Al, Fe, and Si, which were determined to most clearly distinguish the phases, are shown for equivalent regions.

#### 3.2.1. Y-based coating materials

3.2.1.1. Reactions producing Ap, G, and F. The reactions between both Y-based coating materials and the  $C_{15}M_{12}F_{12}A_{16}S_{45}$  deposit (Fig. 4(a,b) produce a thin band of apatite grains at the surface followed by a layer comprising primarily garnet with smaller fractions of apatite and fluorite. The shift in the predominant reaction product is presumably due to the relative depletion of Ca and Si via the initial apatite crystallization, pushing the Al-, Fe-, and Mg-enriched melt into the garnet crystallization field. Although the grain size decreases through the thickness of this layer, the phase assemble doesn't change until the interface with the unreacted material below. Small pockets of glass, which aren't colored in these figures, were present between grains in some places. The EPMA maps show that Zr is concentrated in the fluorite grains, Fe and Al appear primarily in garnet, and Si is concentrated in apatite with lower Si concentration in garnet. Even though the  $C_{15}M_{12}F_{12}A_{16}S_{45}$  deposit has a high Mg and Fe content, intrinsic crystallization products such as

spinel or melilite aren't observed since those cations are accommodated in the garnet phase.

3.2.1.2. Reactions producing Ap, G, F, and Cus. The reactions between the Y-based coating materials and the  $C_{31}M_9F_5A_{12}S_{43}$  deposit (Fig. 4(c, d)) follow the same initial sequence as the  $C_{15}M_{12}F_{12}A_{16}S_{45}$  deposit. An outer layer of apatite transitions to a layer containing primarily garnet with smaller fractions of apatite and fluorite. Closer to the bottom of the reaction layer, apatite disappears and cuspidine becomes the predominant reaction product with smaller fractions of garnet and fluorite. Cuspidine (nominally (Y,Ca)<sub>4</sub>(Al,Si)<sub>2</sub>O<sub>9</sub>) likely appears as enrichment of Ca and Al in the melt shifts the equilibria into a phase field containing it, rather than apatite. The primary difference between the two samples is the position of the transition to cuspidine as the primary reaction product, with the cuspidine comprising approximately one third of the reaction layer thickness for A<sub>10</sub>Y<sub>76</sub>Z<sub>14</sub> but only the bottom one eighth of the reaction layer on  $A_{30}Y_{60}Z_{10}$ . As elaborated in later sections, the compositions of fluorite, cuspidine, and apatite are similar between the samples, but the Al content in the garnet higher for the A<sub>30</sub>Y<sub>60</sub>Z<sub>10</sub> sample.

3.2.1.3. Reactions producing YDS. The reaction of the SiO2-rich

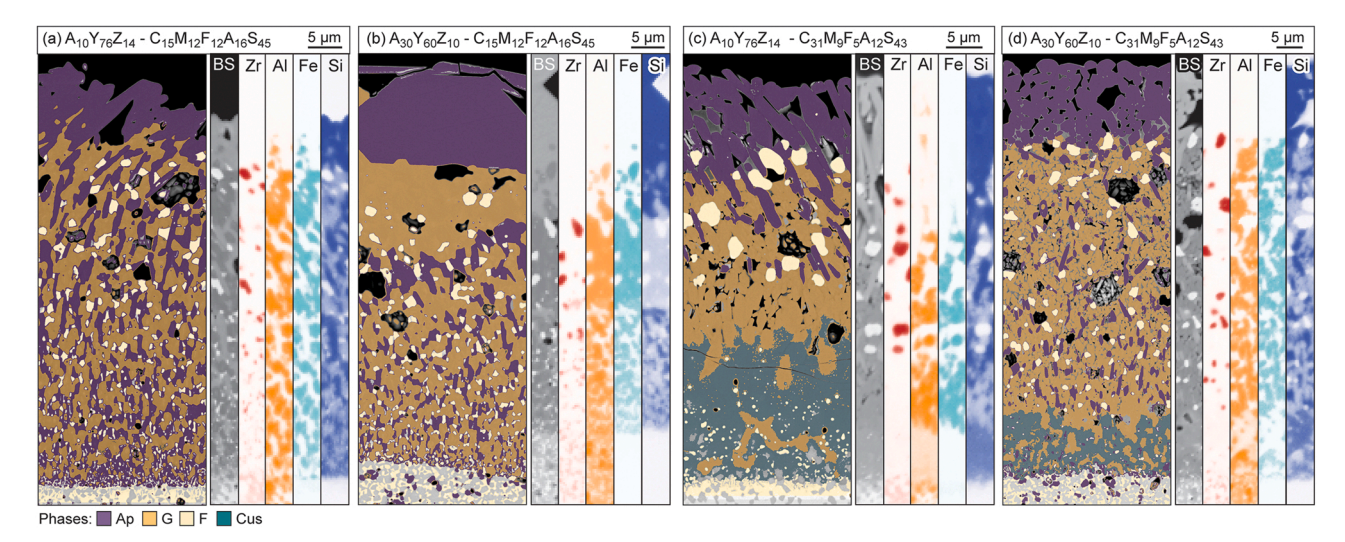


Fig. 4. Reaction layer microstructures taken near the center of the (a)  $A_{10}Y_{76}Z_{14}$  and (b)  $A_{30}Y_{60}Z_{10}$  samples exposed to  $C_{15}M_{12}F_{12}A_{16}S_{45}$  and (c)  $A_{10}Y_{76}Z_{14}$  and (d)  $A_{30}Y_{60}Z_{10}$  exposed to  $C_{31}M_9F_5A_{12}S_{43}$ . The wider image on the left of each panel is a false colored BSE micrograph showing the phase distribution. The narrow images on the right of each panel show selected EPMA data from an equivalent location.

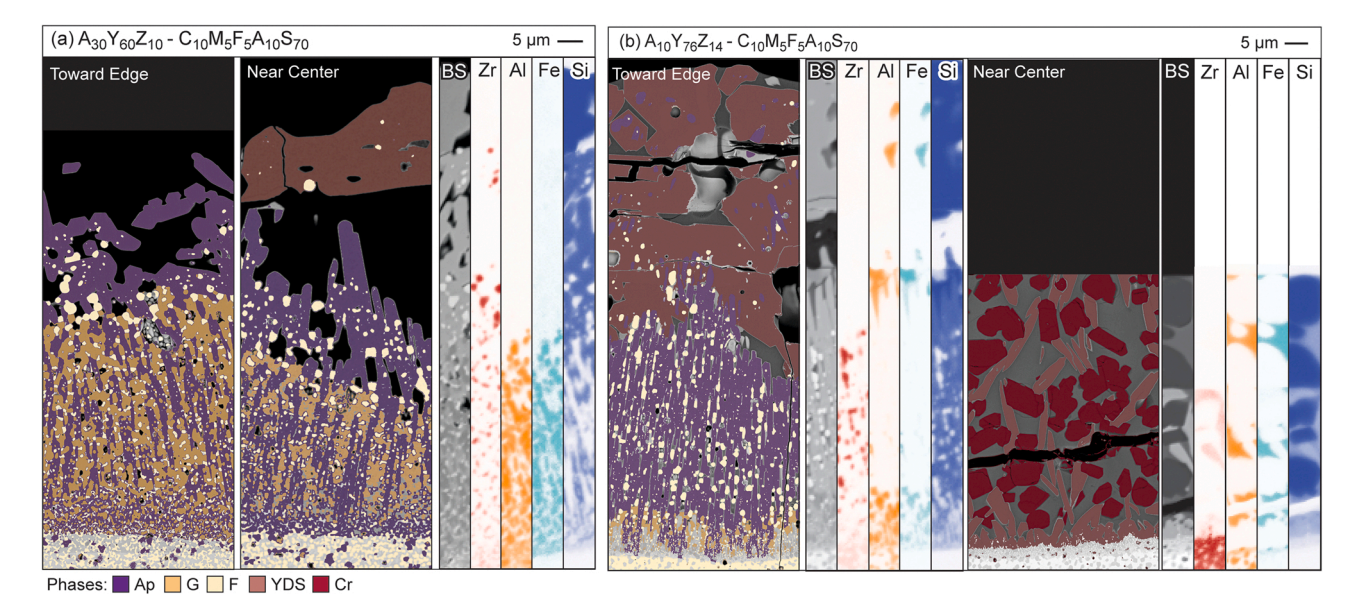


Fig. 5. Reaction layer microstructures observed in the (a)  $A_{30}Y_{60}Z_{10}$  and (b)  $A_{10}Y_{76}Z_{14}$  samples exposed to  $C_{10}M_5F_5A_{10}S_{70}$ . The wider image on the left of each panel is a false colored BSE micrograph showing the phase distribution. The narrow images on the right of each panel show selected EPMA data from an equivalent location.

 $C_{10}M_5F_5A_{10}S_{70}$  with the Y-based coating materials produces YDS along with other reaction products. For  $A_{30}Y_{60}Z_{10}$ , the YDS appears as large (10 s of  $\mu$ m) blocky YDS grains above the center of the primary reaction zone but is absent around the periphery (Fig. 5(a)). The  $A_{10}Y_{76}Z_{14}$  produced a thick reaction layer with large YDS grains around the periphery, with a thinner layer of residual melt containing YDS and cristobalite (SiO<sub>2</sub>) in the center (Fig. 5(b)). The presence of the YDS near the top of the reaction layers, along with its large, blocky morphology, suggest that the YDS precipitates early in the reaction sequence. Once excess SiO<sub>2</sub> from the deposit is consumed via YDS crystallization, the reactions shift into the fields producing a mixture of apatite, garnet, and fluorite.

#### 3.2.2. Gd-based coating materials

3.2.2.1. Reactions producing Ap, G, F, and Sp. The reactions of  $C_{31}M_9F_5A_{12}S_{43}$  with  $A_{10}G_{76}Z_{14}$  and  $C_{15}M_{12}F_{12}A_{16}S_{45}$  with both Gd-based coating materials produce an outer layer of mixed apatite and spinel and an inner layer with mixed apatite and garnet (Fig. 6). Given its high Al content, the spinel location shows clearly in the EPMA maps. Fluorite grains are scattered throughout these layers, but the fluorite fraction is generally much lower than in the Y-based samples due to higher Zr solubility in the garnet phase formed in the Gd-based systems.

3.2.2.2. Reactions producing primarily Ap, G, and F. The reaction layers formed when both Gd-based coating materials react with  $C_{10}M_5F_5A_{10}S_{70}$  comprise layers of apatite, mixed apatite and fluorite, and then mixed apatite, garnet, and fluorite (Fig. 7(a,b)). A band of the Al-rich

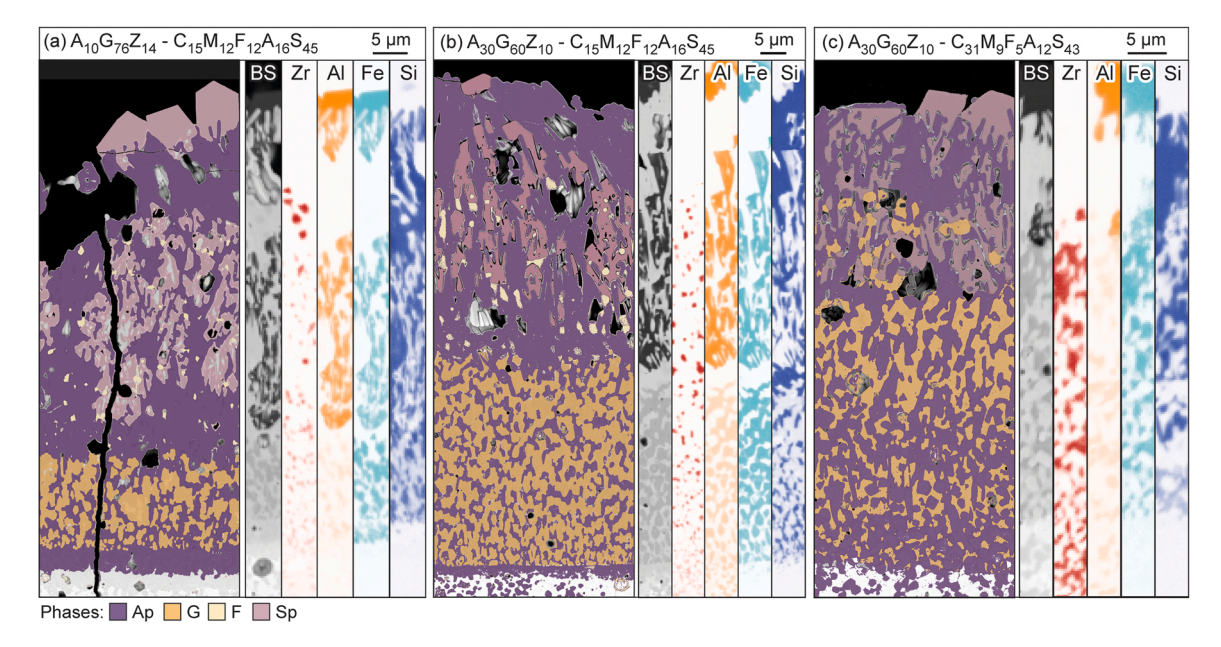


Fig. 6. Reaction layer microstructures observed in the (a)  $A_{10}Y_{76}Z_{14}$  and (b)  $A_{30}Y_{60}Z_{10}$  samples exposed to  $C_{15}M_{12}F_{12}A_{16}S_{45}$  and (c)  $A_{30}Y_{60}Z_{10}$  exposed to  $C_{31}M_9F_5A_{12}S_{43}$ . The wider image in each panel shows the phase distribution and the narrow images show selected EPMA maps from equivalent locations.

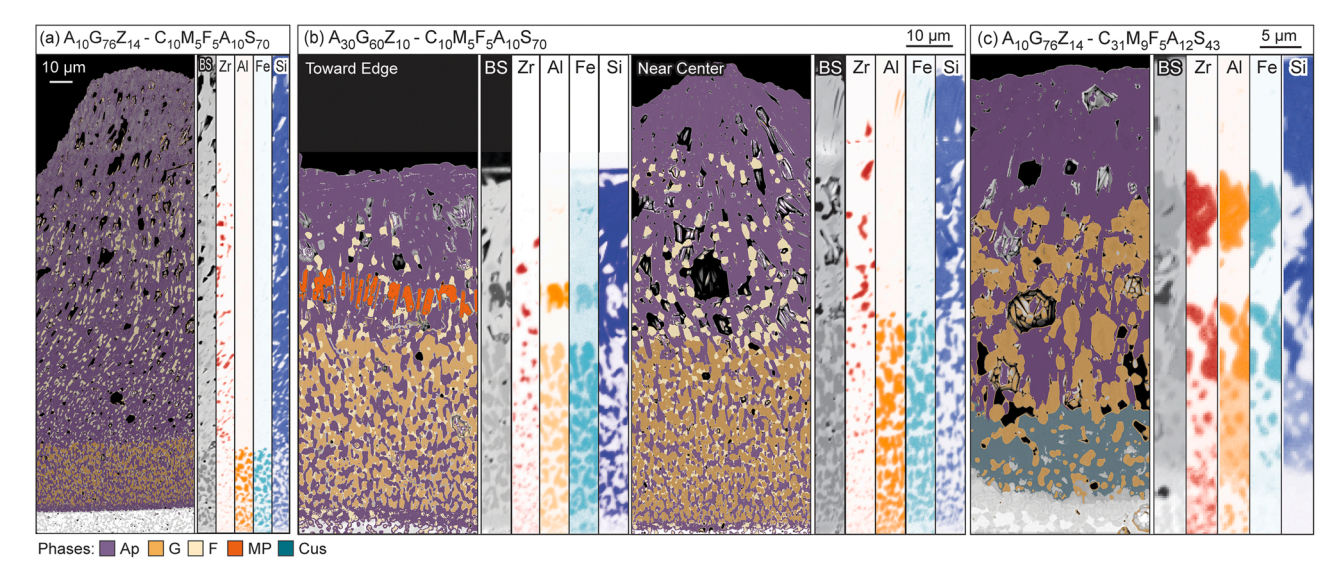


Fig. 7. Reaction layer microstructures observed in the (a)  $A_{10}G_{76}Z_{14}$  and (b)  $A_{30}G_{60}Z_{10}$  samples exposed to  $C_{10}M_5F_5A_{10}S_{70}$  and (c)  $A_{10}G_{76}Z_{14}$  exposed to  $C_{31}M_9F_5A_{12}S_{43}$ .

magnetoplumbite phase appears just above the garnet-containing layer around the periphery of the  $A_{30}G_{60}Z_{10}$  sample. The appearance of garnet later in the sequence compared to the Y-based samples with similar phase assemblages is presumably due to the relatively lower stability of the Gd-containing aluminosilicate garnet.

3.2.2.3. Reactions producing primarily Ap, G, and Cus. The  $\rm A_{10}G_{76}Z_{14}$  sample exposed to  $\rm C_{31}M_9F_5A_{12}S_{43}$  produces a unique reaction sequence. Apatite appears at the top of the reaction layer followed by a region with apatite, garnet, and occasional small periclase grains. The bottom of the reaction layer is primarily cuspidine with interspersed garnet grains. Fluorite isn't evident, presumably because the garnet phase is Zr-rich (along with high Al and Fe content). The garnet and periclase precipitation depletes MgO, pushing the final reaction into a crystallization field involving cuspidine.

#### 3.3. Reaction product composition trends

This section discusses how the reaction product microstructure and compositions change in relation to the coating material and CMFAS compositions.

#### 3.3.1. Apatite

Apatite is formed in all twelve deposit-coating material combinations examined in this study, consistent with its documented formation for various coating materials exposed to a wide range of CMFAS

compositions. The average apatite compositions are given in Table 2. The primary trend is that exposure to the CaO lean  $C_{10}M_5F_5A_{10}S_{70}$  deposits produces apatite with significantly less CaO than the defect-free  $Ca_2RE_8Si_6O_{26}$  stoichiometry. This shift is partially accommodated by increased Mg content, which substitutes for Ca, consistent with observations in related systems [15]. However, even with the MgO substitution, cation vacancies are likely still required for charge balance in these cases [40,41]. The Zr, Al, and Fe content in all apatite measurement is generally low, and is ascribed to a combination of small solubility in apatite and low x-ray signal originating from adjacent grains. There is not a significant difference in the apatite compositions formed on the Gd- vs. Y-containing samples. There is also not significant variation in apatite concentration through the reaction layer in each sample.

#### 3.3.2. Garnet

Garnet is observed in every reaction layer, but the grain sizes, compositions, and relative locations in the reaction layers vary significantly between samples. Although the aluminosilicate garnet phase is unstable at  $1400\,^{\circ}\text{C}$  in the Gd-CMAS system [15], Fe and Zr stabilize the Gd-containing garnet in this study. The through-thickness grain size gradient and configuration relative to other reaction products suggests that the garnet grows at the test temperature during the dynamic dissolution-crystallization process, unlike previous reports that suggested growth of garnet upon cooling [17,23,25]. There was generally not significant variation in the garnet compositions through the thickness of an individual reaction layer, except for a sharp shift toward the

 Table 2

 Average apatite compositions, in cation %, based on EPMA.

Coating material	CMFAS	Si	Zr	Al	RE	Fe	Mg	Ca
A <sub>30</sub> Y <sub>60</sub> Z <sub>10</sub>	$C_{10}M_5F_5A_{10}S_{70}^{a}$	33.5	4.5	0.7	52.5	0.3	1.4	7.1
	$C_{15}M_{12}F_{12}A_{16}S_{45}$	37.0	0.6	0.1	49.3	0.2	1.6	11.2
	$C_{31}M_9F_5A_{12}S_{43}$	35.1	1.3	0.2	48.3	0.1	0.6	14.4
$A_{10}Y_{76}Z_{14}$	$C_{10}M_5F_5A_{10}S_{70}$	35.8	0.3	1.9	50.9	0.6	2.2	8.2
	$C_{15}M_{12}F_{12}A_{16}S_{45}$	38.8	0.5	0.2	47.6	0.2	1.3	11.3
	$C_{31}M_9F_5A_{12}S_{43}$	35.3	0.8	0.2	49.3	0.1	0.5	13.9
$A_{30}G_{60}Z_{10}$	$C_{10}M_5F_5A_{10}S_{70}$	35.7	0.1	1.5	53.4	0.2	2.4	6.7
	$C_{15}M_{12}F_{12}A_{16}S_{45}$	38.6	1.0	1.3	47.0	0.3	1.0	10.9
	$C_{31}M_9F_5A_{12}S_{43}$	37.9	0.8	1.3	45.8	0.2	0.7	13.3
$A_{10}G_{76}Z_{14}$	$C_{10}M_5F_5A_{10}S_{70}$	36.8	0.1	0.8	50.2	0.4	2.8	8.9
	$C_{15}M_{12}F_{12}A_{16}S_{45}$	37.4	0.5	0.4	47.7	0.3	1.8	11.8
	$C_{31}M_9F_5A_{12}S_{43}$	37.9	0.2	0.8	47.2	0.1	0.7	13.1

<sup>&</sup>lt;sup>a</sup> The higher Zr and lower Si content than expected for apatite in this samples is likely due to signal from small fluorite grains embedded within apatite in this sample.

**Table 3** Average garnet compositions (cation %), based on EPMA.

Coating material	CMFAS	Si	Zr	Al	RE	Fe	Mg	Ca
A <sub>30</sub> Y <sub>60</sub> Z <sub>10</sub>	$C_{10}M_5F_5A_{10}S_{70}$	7.3	3.0	46.7	36.9	2.7	2.0	1.3
	$C_{15}M_{12}F_{12}A_{16}S_{45}$	13.1	1.7	31.8	31.9	9.2	7.4	4.9
	$C_{31}M_9F_5A_{12}S_{43}$	14.7	2.9	32.0	27.1	5.7	6.6	10.9
$A_{10}Y_{76}Z_{14}$	$C_{10}M_5F_5A_{10}S_{70}$	14.1	3.8	32.4	38.6	5.7	3.2	2.1
	$C_{15}M_{12}F_{12}A_{16}S_{45}$	17.8	2.3	21.8	30.9	11.6	9.3	6.2
	$C_{31}M_9F_5A_{12}S_{43}$	15.4	4.0	25.9	26.4	8.7	7.8	11.7
$A_{30}G_{60}Z_{10}$	$C_{10}M_5F_5A_{10}S_{70}$	4.3	2.8	51.4	35.6	3.1	2.2	0.6
	$C_{15}M_{12}F_{12}A_{16}S_{45}$	6.0	2.6	43.6	31.9	9.4	3.5	2.9
	$C_{31}M_9F_5A_{12}S_{43}$	5.9	14.1	30.9	24.9	4.4	5.7	14.0
$A_{10}G_{76}Z_{14}$	$C_{10}M_5F_5A_{10}S_{70}$	5.8	3.0	43.0	36.5	7.6	3.7	0.3
	$C_{15}M_{12}F_{12}A_{16}S_{45}$	10.6	5.9	22.6	32.8	17.1	5.5	5.6
	$C_{31}M_9F_5A_{12}S_{43}$	6.6	15.3	23.9	25.6	6.1	7.5	15.0

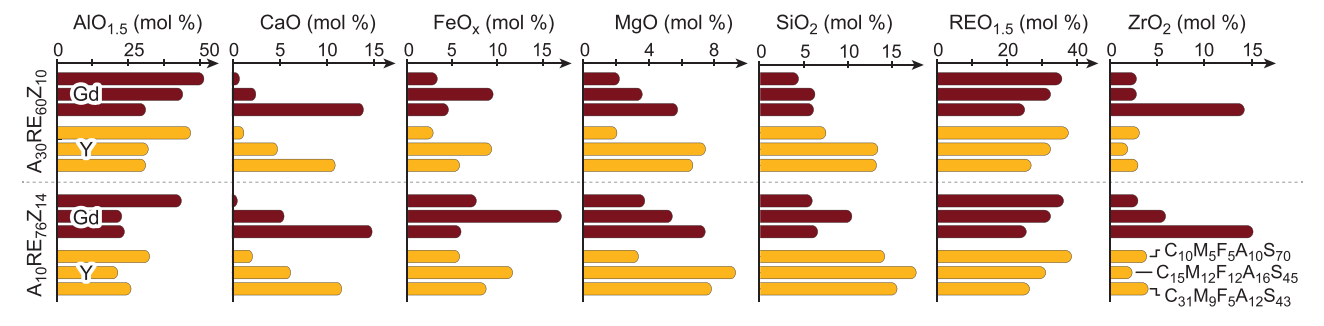


Fig. 8. Average garnet compositions measured in each sample.

pure RE aluminate endmember in the final several grain thicknesses at the bottom of each reaction layer.

The average garnet compositions are tabulated in Table 3 and plotted in Fig. 8. Several trends emerge. First, the Y-based garnets contain roughly twice the SiO<sub>2</sub> content as the garnets formed in the equivalent Gd-based samples, which tended to have higher Al and/or Zr concentrations. Second, the Ca content in the garnet is strongly dependent on the Ca concentration in the deposit. The garnets formed via reactions with  $C_{10}M_5F_5A_{10}S_{70}$  contain almost no Ca, while Ca is a major component in the garnets formed via reactions with  $C_{31}M_9F_5A_{12}S_{43}$ . The low Ca concentrations are accommodated either by substitution of other cations (e.g., Mg, Fe) or by shifting the composition closer to the pure RE aluminate endmember since RE and Ca cations occupy the same crystallographic site. Similarly, exposure to the Fe-rich  $C_{15}M_{12}F_{12}A_{16}S_{45}$  deposit produces garnet with higher  $Fe^{2+/3+}$  content. Finally, the garnets formed upon reaction with the  $A_{30}RE_{60}Z_{10}$  materials tended to have higher Al concentration than that formed by reaction with  $A_{10}RE_{76}Z_{14}$ .

In addition to the trends of garnet compositions reflecting variations in CMFAS and coating material compositions, some of these trends can

be explained based on the relative position of the garnet in the reaction sequence. For instance, stronger apatite formation in the Gd based systems consumes significant proportions of Si and Ca from the deposit. Consequently, the garnet, which formed later in these samples, has less Si and more Zr. In other cases, consumption of Mg, Fe, and Al via early spinel formation leads to garnet crystallization with more Si and Zr in the local equilibrium environment.

#### 3.3.3. Fluorite

Fluorite is observed in the reaction layer in all Y-containing samples but only some Gd-containing samples since Zr is more readily incorporated in the Gd-containing garnet. The fluorite is essentially RE-stabilized ZrO<sub>2</sub>, but with lower RE content than the starting materials, and with only small CaO concentrations (Table 4). In some cases, the grains were sufficiently small to cause overlap with signal originating from adjacent grains. This is most evident in the unphysically high Si content reported for some samples. For equivalent samples, the Gd content is fluorite is lower than the Y content in the corresponding sample, consistent with cation size dependent partitioning trends [32].

**Table 4**Average fluorite compositions (cation %) before and after CMFAS exposure.

Coating material	CMFAS	Si	Zr	Al	RE	Fe	Mg	Ca
$A_{30}Y_{60}Z_{10}$	Initial <sup>a</sup>	-	45.6	0.2	54.2	-	-	-
	$C_{10}M_5F_5A_{10}S_{70}$	1.6	64.5	0.3	32.7	0.6	0.1	0.3
	$C_{15}M_{12}F_{12}A_{16}S_{45}$	1.6	62.0	3.3	29.5	1.8	0.9	0.9
	$C_{31}M_9F_5A_{12}S_{43}$	2.4	57.8	1.4	33.8	0.8	0.7	3.1
$A_{10}Y_{76}Z_{14}$	Initial	-	52.2	0.3	47.6	-	-	-
	$C_{10}M_5F_5A_{10}S_{70}$	5.7	57.6	0.5	33.7	1.0	0.3	1.2
	$C_{15}M_{12}F_{12}A_{16}S_{45}$	1.9	64.7	1.2	28.3	2.4	0.7	0.8
	$C_{31}M_9F_5A_{12}S_{43}$	1.0	58.5	0.2	36.5	0.9	0.6	2.4
$A_{30}G_{60}Z_{10}$	Initial	-	32.2	0.1	67.7	-	-	-
	$C_{10}M_5F_5A_{10}S_{70}$	0.5	67.3	0.4	30.7	0.5	0.4	0.1
	$C_{15}M_{12}F_{12}A_{16}S_{45}$	3.5	62.3	0.5	29.4	1.7	0.6	2.0
$A_{10}G_{76}Z_{14}$	Initial	-	46.0	0.3	53.6	-	-	-
	$C_{10}M_5F_5A_{10}S_{70}$	2.0	66.8	0.5	28.6	1.0	0.6	0.5
	$C_{15}M_{12}F_{12}A_{16}S_{45}$	5.7	58.2	0.5	28.9	2.4	1.1	3.2

<sup>&</sup>lt;sup>a</sup> Fluorite composition in the initial, unreacted material

**Table 5**Average compositions of cuspidine and spinel, in cation %.

Coating material	CMFAS	Si	Zr	Al	RE	Fe	Mg	Ca
Cuspidine								
$A_{30}Y_{60}Z_{10}$	$C_{31}M_9F_5A_{12}S_{43}$	23.5	5.8	9.1	32.6	0.5	1.4	27.0
$A_{10}Y_{76}Z_{14}$	$C_{31}M_9F_5A_{12}S_{43}$	24.3	5.4	7.6	33.9	0.8	1.6	26.6
$A_{10}G_{76}Z_{14}$	$C_{31}M_9F_5A_{12}S_{43}$	21.1	3.0	12.9	40.6	0.8	1.1	20.4
Spinel								
$A_{30}G_{60}Z_{10}$	$C_{15}M_{12}F_{12}A_{16}S_{45}$	0.8	0.2	62.6	1.2	7.4	27.4	0.4
	$C_{31}M_9F_5A_{12}S_{43}$	0.8	0.0	63.1	0.8	3.2	31.7	0.3
$A_{10}G_{76}Z_{14}$	$C_{15}M_{12}F_{12}A_{16}S_{45}$	5.2	1.3	42.2	8.1	11.9	29.3	2.1

#### 3.3.4. Spinel

Spinel based on MgAl $_2$ O $_4$  with modest Fe solubility (Table 5) appeared in equilibrium with apatite, fluorite, and garnet early in the reaction sequence for the Gd-containing systems. Its appearance coincided with either higher Al content in the coating material ( $A_{30}G_{60}Z_{10}$ ), or higher Al, Mg, and Fe from the  $C_{15}M_{12}F_{12}A_{16}S_{45}$  deposit. The spinel in the latter cases contained proportionally more Fe, consistent with the relative cation proportions in the coating material and deposit. The corresponding Y-containing samples did not form spinel, likely because the Mg, and Fe are accommodated in the silica-rich garnet [15,16,25,32] more readily than in the Zr-rich garnet formed in the Gd samples.

#### 3.3.5. Cuspidine

Cuspidine was observed in three cases when the coating materials were exposed to the CaO-rich  $C_{31}M_9F_5A_{12}S_{43}$  (Table 5). It forms in equilibrium with garnet and fluorite in a dense zone close to the unreacted coating material. The cuspidine conforms to the nominal stoichiometry (Ca,RE)\_4(Al,Si)\_2O\_9. The cuspidine formed on the two Y-based materials is relatively Ca- and Si- rich, closer to the  $Ca_2Y_2Si_2O_9$  endmember than to the  $Y_4Al_2O_9$  endmember. The cuspidine formed on  $A_{10}G_{76}Z_{14}$  contains slightly less Ca and Si (with more Al and RE). These compositions are generally like those formed in Yb-based coating materials exposed to a similar deposit composition [32].

#### 3.3.5.1. Magnetoplumbite. Magnetoplumbite with a nominal

stoichiometry of  $GdMgAl_{11}O_{19}$  [42] appears at the periphery of the  $A_{30}G_{60}Z_{10}$  samples exposed to  $C_{10}M_5F_5A_{10}S_{70}$  and  $C_{15}M_{12}F_{12}A_{16}S_{45}$ . The phase has modest  $FeO_x$  and CaO solubility, and forms in equilibrium with apatite and fluorite (along with some spinel) in the  $A_{30}G_{60}Z_{10}$ - $C_{15}M_{12}F_{12}A_{16}S_{45}$  sample. As an Al-rich phase, magneto-plumbite formation is promoted by the presence of alumina in the coating materials.

#### 3.4. Reactive crystallization efficiency

The alumina in these aluminate-zirconate coating materials promotes diverse reaction products with varying ability to efficiently consume the melt. The reactive efficiencies  $(\eta)$  calculated based on the average composition of each phase in each sample are plotted in Fig. 9 (a). The results show that fluorite, magnetoplumbite, and GAP form by reprecipitation, with  $\eta<0.15$ . Conversely, the cuspidine, YDS, and apatite values are clustered near  $\eta=0.5$ , indicating more efficient reactive crystallization. The garnet compositions span a wide range of intermediate values. However, garnet crystallization in the current experiments is generally less efficient than for the pure zirconates and hafnates (Fig. 1), since incorporation of alumina from the coating material reduced deposit consumption.

To understand the interplay between the coating material and deposit composition on the garnet reaction efficiency, the garnet crystallization efficiencies for each sample are plotted separately in Fig. 9(b).

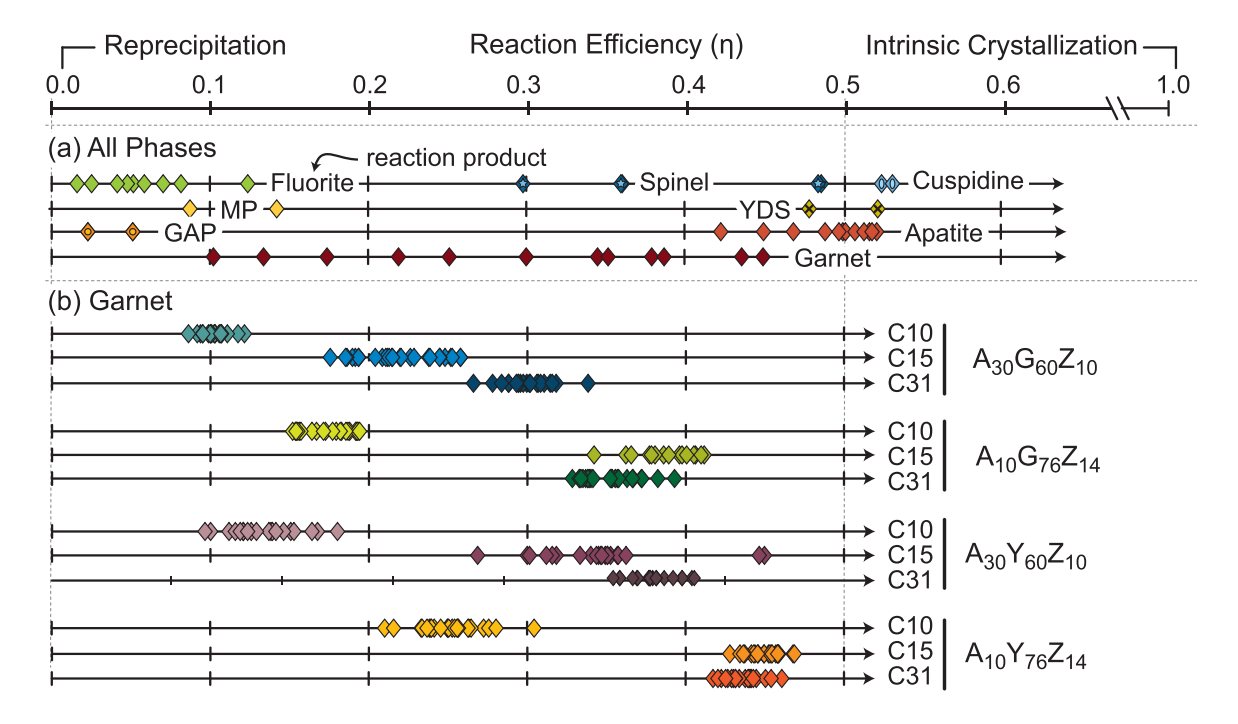


Fig. 9. Reaction efficiency parameters based on (a) average composition of each phase in each sample and (b) individual points for each garnet grain measured. Abbreviations:  $C10 = C_{10}M_5F_5A_{10}S_{70}$ ,  $C15 = C_{15}M_{12}F_{12}A_{16}S_{45}$ , and  $C31 = C_{31}M_9F_5A_{12}S_{43}$ .

Several trends are evident. First, the garnet formed upon exposure of each coating material to  $C_{10}M_5F_5A_{10}S_{70}$  has a lower reaction efficiency (closer to reprecipitation) than the other deposits. This is because without ample Ca, Mg, and Fe from the deposit to charge compensate Si incorporation into garnet, the garnet more closely resembles an aluminate, rather than an aluminosilicate. Second, garnet formation with the  $AlO_{1.5}$ -rich  $A_{30}RE_{60}Z_{10}$  has lower reaction efficiency than the equivalent  $A_{10}RE_{76}Z_{14}$ , implying that even if the  $AlO_{1.5}$  in the coating material can promote garnet crystallization, the lower efficiency of that reaction may not offer a net benefit for consuming the melt. Finally, because Y better stabilizes garnets containing higher concentrations of Mg, Fe, Ca, and Si, garnet crystallization with the Y-containing coating materials is more efficient than the Gd-containing materials.

## 3.5. Implications for the design of multiphase aluminate zirconate coating materials

The results show that the introduction of one or more RE aluminates into a RE zirconate coating material promotes the formation of garnet and cuspidine, in addition to apatite, upon reaction with CMFAS deposits. A potential benefit of this approach is a more uniform reaction response across a range of CMFAS deposit compositions leading to effective melt consumption even if one or more reactants is consumed. Specifically, this work shows that once apatite crystallization early in the reaction sequence consumes Ca and Si, the Al liberated from the coating material promotes garnet crystallization to continue consuming the remaining melt later in the reaction sequence. This translates to a more efficient redistribution and consumption of melt across the coating-CMFAS reaction layer. Additionally, since Y is particularly effective in promoting garnet crystallization, the use of an aluminatecontaining, Y-based coating material could offset the lower driving force for apatite crystallization compared to Gd. This characteristic opens potential for coating materials to offer the desired performance while using the more abundant and lower cost Y rather than Gd.

At the same time, the addition of alumina to the coating material decreases the efficiency of the garnet crystallization reaction since a portion of the Al in the garnet comes from the dissolved coating material. In other words, more coating material must dissolve to consume an equivalent quantity of melt compared to the garnet reactions products formed by RE zirconate materials (Fig. 1). This is especially true for the Gd-based materials since the equivalent Y-containing garnets show more efficient melt consumption.

Based on observations of uniformity in reaction sequences, melt consumption efficiency of formed crystalline products, and the overall uniformity in reaction layer thicknesses, multiphase aluminate zirconates are promising candidates as CMFAS-reactive coating materials. This is particularly true for applications where the material serves as a sacrificial layer for CMFAS protection, since exfoliation of thin, uniform reaction layers could remove the deposit while leaving the rest of the coating intact.

#### 4. Conclusions

The sequence and chemistry of the products of reactions between silicate melts and mixed Gd and Y aluminate-zirconate candidate coating materials was studied. Key conclusions include:

- The coating materials studied react quickly with CMFAS deposits to form a variety of crystalline products. Apatite and garnet phases formed in every reaction layer and fluorite formed in most reaction layers. Other reaction products include cuspidine, YDS, spinel, cristobalite, magnetoplumbite, and periclase.
- The most common reaction progression involves an outer layer of apatite with fluorite and garnet appearing in conjunction with apatite below the surface. In some cases, spinel is intermixed with apatite at the top of the reaction layer, and in other cases a layer of

- predominantly cuspidine appears at the bottom of the reaction layer. YDS appears either as large blocky grains at the surface of the reaction layer or suspended in the residual melt (glass).
- 3. The garnet formed in the Y-containing samples typically contained 13–18 mol% SiO<sub>2</sub>, which is about half of the maximum SiO<sub>2</sub> solubility in the phase, with corresponding CaO and MgO to maintain charge neutrality. The garnets formed in the Gd systems contained more ZrO<sub>2</sub> and less SiO<sub>2</sub> than the equivalent Y systems.
- 4. The melt consumption efficiency  $(\eta)$  for apatite, cuspidine, and YDS are clustered near 0.5, making them ideal reactive crystallization products, while fluorite is closer to reprecipitation. The garnet crystallization efficiency spans an intermediate range depending on the RE cation and the CMFAS composition.

#### **Declaration of Competing Interest**

The authors declare that they have no known competing financial interests or personal relationships that could have appeared to influence the work reported in this paper.

#### Acknowledgements

This research was supported by the NASA award number 80NSSC21C0071 monitored by Dr. Cameron Bodenschatz, in collaboration with QuesTek Innovations LLC. N.H. was supported by the NSF REU program under Award Number DMR-1852044 and through the University of Minnesota MRSEC under Award Number DMR-2011401. Part of this work was carried out in the Characterization Facility at the University of Minnesota, which receives partial support from the NSF through the MRSEC (DMR-2011401) and the NNCI (ECCS-2025124) programs. The sponsors were not involved in the detailed study design, or the data collection, analysis, or interpretation. The authors are grateful to Drs. Noriaki Arai, Pin Lu, and Jiadong Gong (QuesTek Innovations LLC) for the insightful discussions.

#### Appendix A. Supporting information

Supplementary data associated with this article can be found in the online version at <a href="doi:10.1016/j.jeurceramsoc.2023.05.009">doi:10.1016/j.jeurceramsoc.2023.05.009</a>.

#### References

- D.L. Poerschke, R.W. Jackson, C.G. Levi, Silicate deposit degradation of engineered coatings in gas turbines: progress toward models and materials solutions, Annu Rev. Mater. Res. 47 (2017) 297–330, https://doi.org/10.1146/annurev-matsci-010917-105000.
- [2] N.P. Padture, Thermal barrier coatings for gas-turbine engine applications, Science 80 (296) (2002) 280–284. https://doi.org/10.1126/science.1068609.
- [3] D.R. Clarke, C.G. Levi, Materials design for the next generation thermal barrier coatings, Annu Rev. Mater. Res 33 (2003) 383–417, https://doi.org/10.1146/ annurev.matsci.33.011403.113718.
- [4] C.G. Levi, J.W. Hutchinson, M.-H. Vidal-Sétif, C.A. Johnson, Environmental degradation of thermal-barrier coatings by molten deposits, MRS Bull. 37 (2012) 932–941, https://doi.org/10.1557/mrs.2012.230.
- [5] F.H. Stott, D.J. de Wet, R. Taylor, Degradation of thermal-barrier coatings at very high temperatures, MRS Bull. 19 (1994) 46–49, https://doi.org/10.1557/ S0883766400048223
- [6] M.P. Borom, C.A. Johnson, L.A. Peluso, Role of environmental deposits and operating surface temperature in spallation of air plasma sprayed thermal barrier coatings, Surf. Coatings Technol. 86–87 (1996) 116–126, https://doi.org/10.1016/ S0257-8972(96)02994-5.
- [7] W. Song, Y. Lavallee, K.U. Hess, U. Kueppers, C. Cimarelli, D.B. Dingwell, Volcanic ash melting under conditions relevant to ash turbine interactions, Nat. Commun. 7 (2016) 1–10, https://doi.org/10.1038/ncomms10795.
- [8] J. Elms, A. Pawley, N. Bojdo, M. Jones, R. Clarkson, The formation of high temperature minerals from an evaporite-rich dust in gas turbine engine ingestion tests, Proc. ASME Turbo Expo. 2B-2020 (2020) 1–11, https://doi.org/10.1115/ GT2020-14236.
- [9] S. Krämer, J. Yang, C.G. Levi, Infiltration-inhibiting reaction of gadolinium zirconate thermal barrier coatings with CMAS melts, J. Am. Ceram. Soc. 91 (2008) 576–583, https://doi.org/10.1111/j.1551-2916.2007.02175.x.

- [10] D.R. Clarke, M. Oechsner, N.P. Padture, Thermal-barrier coatings for more efficient gas-turbine engines, MRS Bull. 37 (2012) 891–898, https://doi.org/10.1557/ mrs 2012 232
- [11] E.J. Gildersleeve, S. Sampath, Dynamic interactions of ingested molten silicate particles with air plasma sprayed thermal barrier coatings, J. Mater. Res 35 (2020) 2321–2334, https://doi.org/10.1557/jmr.2020.196.
- [12] D. Müller, K.U. Hess, U. Kueppers, S. Lokachari, D.B. Dingwell, G. Wolf, et al., Rheological and chemical interaction between volcanic ash and thermal barrier coatings, Surf. Coat. Technol. 412 (2021), 127049, https://doi.org/10.1016/j. surfcoat.2021.127049.
- [13] E. Gildersleeve, V. Viswanathan, S. Sampath, Molten silicate interactions with plasma sprayed thermal barrier coatings: Role of materials and microstructure, J. Eur. Ceram. Soc. 39 (2019) 2122–2131, https://doi.org/10.1016/j. jeurceramsoc.2019.01.023.
- [14] R.W. Jackson, E.M. Zaleski, B.T. Hazel, M.R. Begley, C.G. Levi, Response of molten silicate infiltrated Gd<sub>2</sub>Zr<sub>2</sub>O<sub>7</sub> thermal barrier coatings to temperature gradients, Acta Mater. 132 (2017) 538–549. https://doi.org/10.1016/j.actamat.2017.03.081.
- [15] E. Godbole, A. von der Handt, D. Poerschke, Apatite and garnet stability in the Al-Ca-Mg-Si-(Gd/Y/Yb)-O systems and implications for T/EBC: CMAS reactions, J. Am. Ceram. Soc. 105 (2022) 1596–1609, https://doi.org/10.1111/jace.18179.
- [16] E. Godbole, N. Karthikeyan, D. Poerschke, Garnet stability in the Al-Ca-Mg-Si-Y-O system with implications for reactions between TBCs, EBCs, and silicate deposits, J. Am. Ceram. Soc. 103 (2020) 5270–5282, https://doi.org/ 10.1111/jace.17176.
- [17] D.L. Poerschke, D.D. Hass, S. Eustis, G.G.E. Seward, J.S. Van Sluytman, C.G. Levi, Stability and CMAS resistance of ytterbium-silicate/hafnate EBCs/TBC for SiC composites, J. Am. Ceram. Soc. 98 (2015) 278–286, https://doi.org/10.1111/ iace\_13262
- [18] D.L. Poerschke, G.G.E. Seward, C.G. Levi, Influence of Yb:Hf ratio on ytterbium hafnate/molten silicate (CMAS) reactivity, J. Am. Ceram. Soc. 99 (2016) 651–659, https://doi.org/10.1111/jace.13964.
- [19] A.R. Krause, H.F. Garces, C.E. Herrmann, N.P. Padture, Resistance of 2ZrO<sub>2</sub>·Y<sub>2</sub>O<sub>3</sub> top coat in thermal/environmental barrier coatings to calcia-magnesia-aluminosilicate attack at 1500°C, J. Am. Ceram. Soc. 100 (2017) 3175–3187, https://doi.org/10.1111/jace.14854.
- [20] L.R. Turcer, A.R. Krause, H.F. Garces, L. Zhang, N.P. Padture, Environmental-barrier coating ceramics for resistance against attack by molten calcia-magnesia-aluminosilicate (CMAS) glass: part I, YAlO<sub>3</sub> and γ-Y<sub>2</sub>Si<sub>2</sub>O<sub>7</sub>, J. Eur. Ceram. Soc. 38 (2018) 3905–3913. https://doi.org/10.1016/j.jeurceramsoc.2018.03.021.
- [21] J.J.G. Chavez, R. Naraparaju, C. Mikulla, P. Mechnich, K. Kelm, C.V. Ramana, et al., Comparative study of EB-PVD gadolinium-zirconate and yttria-rich zirconia coatings performance against Fe-containing calcium-magnesium-aluminosilicate (CMAS) infiltration, Corros. Sci. (2021), 109660, https://doi.org/10.1016/j.corsci.2021.109660.
- [22] J.J. Gomez Chavez, R. Naraparaju, P. Mechnich, K. Kelm, U. Schulz, C.V. Ramana, Effects of yttria content on the CMAS infiltration resistance of yttria stabilized thermal barrier coatings system, J. Mater. Sci. Technol. 43 (2020) 74–83, https:// doi.org/10.1016/j.jmst.2019.09.039.
- [23] N.K. Eils, P. Mechnich, W. Braue, Effect of CMAS deposits on MOCVD coatings in the system Y<sub>2</sub>O<sub>3</sub>-ZrO<sub>2</sub>: phase relationships, J. Am. Ceram. Soc. 96 (2013) 3333–3340, https://doi.org/10.1111/jace.12502.
- [24] P. Mechnich, W. Braue, U. Schulz, High-temperature corrosion of EB-PVD yttria partially stabilized zirconia thermal barrier coatings with an artificial volcanic ash overlay, J. Am. Ceram. Soc. 94 (2011) 925–931, https://doi.org/10.1111/j.1551-2916.2010.04166 x
- [25] D.L. Poerschke, T.L. Barth, C.G. Levi, Equilibrium relationships between thermal barrier oxides and silicate melts, Acta Mater. 120 (2016) 302–314, https://doi.org/ 10.1016/j.actamat.2016.08.077.

- [26] W.D. Summers, D.L. Poerschke, A.A. Taylor, A.R. Ericks, C.G. Levi, F.W. Zok, Reactions of molten silicate deposits with yttrium monosilicate, J. Am. Ceram. Soc. (2019) 2919–2932, https://doi.org/10.1111/jace.16972.
- [27] A.R. Krause, H.F. Garces, B.S. Senturk, N.P. Padture, 2ZrO<sub>2</sub>·Y<sub>2</sub>O<sub>3</sub> thermal barrier coatings resistant to degradation by molten CMAS: part II, interactions with sand and fly ash, J. Am. Ceram. Soc. 97 (2014) 3950–3957, https://doi.org/10.1111/jace.13209.
- [28] D.L. Poerschke, J.H. Shaw, N. Verma, F.W. Zok, C.G. Levi, Interaction of yttrium disilicate environmental barrier coatings with calcium-magnesium-iron aluminosilicate melts, Acta Mater. 145 (2018) 451–461, https://doi.org/10.1016/j. actamat.2017.12.004.
- [29] S. Krämer, J. Yang, C.G. Levi, Infiltration-inhibiting reaction of gadolinium zirconate thermal barrier coatings with CMAS melts, J. Am. Ceram. Soc. 91 (2008) 576–583, https://doi.org/10.1111/j.1551-2916.2007.02175.x.
- [30] M.P. Schmitt, S.P. Stepanoff, A.K. Rai, P.E. Lauer, R.W. Spangler, D.E. Wolfe, Enhanced calcium–magnesium–aluminosilicate (CMAS) resistance of GdAlO<sub>3</sub> (GAP) for composite thermal barrier coatings, J. Am. Ceram. Soc. 105 (2022) 4435–4448, https://doi.org/10.1111/jace.18408.
- [31] R. Naraparaju, J.J. Gomez Chavez, U. Schulz, C.V. Ramana, Interaction and infiltration behavior of Eyjafjallajökull, Sakurajima volcanic ashes and a synthetic CMAS containing FeO with/in EB-PVD ZrO<sub>2</sub> -65 wt% Y<sub>2</sub>O<sub>3</sub> coating at high temperature, Acta Mater. 136 (2017) 164–180, https://doi.org/10.1016/j. actamat.2017.06.055.
- [32] D.L. Poerschke, C.G. Levi, Effects of cation substitution and temperature on the interaction between thermal barrier oxides and molten CMAS, J. Eur. Ceram. Soc. 35 (2015) 681–691, https://doi.org/10.1016/j.jeurceramsoc.2014.09.006.
- [33] Godbole E.P., Hewage N., Poerschke D.L. Understanding the CMFAS melt spreading and reaction behavior with multiphase rare earth aluminate zirconate candidate thermal and environmental barrier coating materials. Manuscript under review.
- [34] A.R. Ericks, F.W. Zok, D.L. Poerschke, C.G. Levi, Protocol for selecting exemplary silicate deposit compositions for evaluating thermal and environmental barrier coatings, J. Am. Ceram. Soc. 105 (2022) 3665–3688, https://doi.org/10.1111/ jace.18413.
- [35] Y. Yu, E.P. Godbole, et al., Slow sintering in garnet-containing Y and Gd zirconate aluminate mixtures for thermal barrier coatings In Press (2023), https://doi.org/ 10.1111/jace.19121.
- [36] J.J. Donovan, J.W. Singer, J.T. Armstrong, A new EPMA method for fast trace element analysis in simple matrices, Am. Miner. 101 (2016) 1839–1853, https://doi.org/10.2138/am-2016-5628.
- [37] J.J. Donovan, J.M. Allaz, A.Von Der Handt, G.G.E. Seward, O. Neill, K. Goemann, et al., Quantitative WDS compositional mapping using the electron microprobe, Am. Miner. 106 (2021) 1717–1735, https://doi.org/10.2138/am-2021-7739.
- [38] J.J. Donovan, T.N. Tingle, An improved mean atomic number background correction for quantitative microanalysis, Microsc. Micro 2 (1996) 1–7, https://doi.org/10.1017/\$1431927696210013.
- [39] Donovan J.J. Probe for EPMA  $\langle http://www.probesoftware.com/ \rangle$ .
- [40] D.L. Poerschke, T.L. Barth, O. Fabrichnaya, C.G. Levi, Phase equilibria and crystal chemistry in the calcia-silica-yttria system, J. Eur. Ceram. Soc. 36 (2016) 1743–1754, https://doi.org/10.1016/j.jeurceramsoc.2016.01.046.
- [41] D.L. Poerschke, C.G. Levi, Phase equilibria in the calcia-gadolinia-silica system, J. Alloy. Compd. 695 (2017) 1397–1404, https://doi.org/10.1016/j. iallcom 2016 10 263
- [42] N.P. Bansal, D. Zhu, Thermal properties of oxides with magnetoplumbite structure for advanced thermal barrier coatings, Surf. Coat. Technol. 202 (2008) 2698–2703, https://doi.org/10.1016/j.surfcoat.2007.09.048.